Composite Structures 241 (2020) 112125

Contents lists available at ScienceDirect

Composite Structures

journal homepage: www.elsevier.com/locate/compstruct

A physically-based failure analysis framework for fiber-reinforced composite laminates under multiaxial loading

Jian Deng[a,b], Zhenjun Hong[d,e], Qiaozhi Yin[a,c], Tian Jian Lu[a,b,f,*]

[a] State Key Laboratory of Mechanics and Control of Mechanical Structures, Nanjing University of Aeronautics and Astronautics, 210016 Nanjing, China
[b] Nanjing Center for Multifunctional Lightweight Materials and Structures, Nanjing University of Aeronautics and Astronautics, 210016 Nanjing, China
[c] Key Laboratory of Fundamental Science for National Defense-Advanced Design Technology of Flight Vehicle, Nanjing University of Aeronautics and Astronautics, 210016 Nanjing, China
[d] Material Science and Engineering Institute, Shanghai Jiao Tong University, 200240 Shanghai, China
[e] Institute of Technology, Inner Mongolia First Machinery Group Corporation, 014030 Baotou, China
[f] State Key Laboratory for Strength and Vibration of Mechanical Structures, Xi'an Jiaotong University, 710049 Xi'an, China

ARTICLE INFO

Keywords:
Composite laminates
Failure criteria
Strengths
Fracture plane

ABSTRACT

Fiber reinforced composites are widely accepted as efficient alternatives for designing light-weight and high-performance structures, yet theoretical prediction of failure for such composites is still a challenging task with uncertainties and controversies. In this work, a new physically-based failure analysis framework is proposed to predict both intralaminar failure onset and strengths for composite laminates under general stress states, with interactive and coupling effects of stresses fully considered. The *in situ* strengths are introduced using the simplified fracture mechanics-based approximation formula where the constraining effects of both the adjacent plies and embedded laminar thickness are considered. The proposed framework is validated by comparing predictions with existing experimental data. Both initial and final failure envelopes are well predicted for unidirectional and multi-directional laminates under multiaxial loads. Stress-strain responses are also well captured, further illustrating the influence of *in situ* strengths on failure initiation.

1. Introduction

Fiber reinforced composites are widely accepted as efficient alternatives of conventional metal materials for designing structures with light weight and high performance. With the cost reduced by advanced manufacturing techniques, carbon and glass fiber reinforced plastics (CFRP, GFRP) are highly demanded in a wide range of industries ranging from aerospace, naval vehicles, auto-mobile and civil construction to mention a few. However, at present, composite laminated structures are generally over-designed to ensure reliable structural performance, as theoretical predictive models of damage and failure mechanisms in composites have not been fully established yet and are still under development. Uncertainties and controversies remain despite of large efforts devoted to this subject [1–13].

During the continuous development of failure criteria for composite laminates in the last thirty years, two main divisions are classified, namely, non-physically based and physically based criteria. Initiated by von Mises stress theory of isotropic materials, a composite laminate is considered as a single orthotropic material in non-physically based criteria. They are usually formulated in uniform polynomials [3,14], so that local failure mechanisms are not considered under combined stress states, thus enhancing the efficiency in damage tolerance assessment during the preliminary design stage of composite structures. On the other hand, the physically based criteria are generally formulated with separated expressions, accounting for different failure mechanisms. For this reason, more detailed information of local damage can be provided. Specifically, intralaminar failure of composite laminates can be mainly divided into longitudinal failure (e.g., fiber rupture and kinking) and transverse or inter-fiber failure which is mostly initiated by matrix cracking.

Hashin [1,15] initiated the work on physical based failure criteria and introduced interactive criteria to directly determine the failure modes for unidirectional (UD) laminates. Most successive failure theories more or less referred to Hashin's work, but the stress interactions do not always correlate well with experimental data, especially for transverse matrix failure [3,16]. On the basis of Mohr-Coulomb fracture theory and existing knowledge on damage mechanisms, Puck and co-authors [2,17] proposed the concept of fracture plane and fracture

* Corresponding author at: State Key Laboratory of Mechanics and Control of Mechanical Structures, Nanjing University of Aeronautics and Astronautics, 210016 Nanjing, China.
E-mail address: tjlu@nuaa.edu.cn (T.J. Lu).

https://doi.org/10.1016/j.compstruct.2020.112125
Received 22 December 2019; Received in revised form 20 February 2020; Accepted 24 February 2020
Available online 26 February 2020

angle to particularly deal with transverse compression failure. During the three times of World-Wide Failure Exercises (WWFE), the fracture plane concept was highly recommended by many researchers for predicting inter-fiber failure of laminates under combined stresses [3–5,18]. Davila et al. [7] further developed a novel analysis framework for predicting the intralaminar failure of UD laminates based on Hashin's interactive stress theory and Puck's fracture plane concept.

Given that the initial geometric configurations of laminates are thin and slender, the plane stress hypothesis has been extensively employed. However, three dimensional stress states are more practically applied where the out-of-plane stresses play an important role in failure initiation of laminated structures [6,19]. This is due to the fact that general stress states are quite common in multi-directional engineering structures having geometric discontinuities, e.g., free edges, open holes and inserts, asymmetric stiffened and sandwich panels. On the other hand, the basic linear form of Puck's theory was preferred to establish failure analysis strategies. Nevertheless, further investigations showed that the predicted strengths using the linear form were generally greater than experimental data, especially for the case under high compressive load [4]. To handle these general stress states and limitations, improvements and extensions in failure modeling frameworks were further advanced, with additional consideration on material properties and geometric information using the concept of fracture plane [12,20].

It should be mentioned that most recent failure models adopted the maximum stress or strain criterion to address fiber tensile failure due to its simplicity and applicability. However, its prediction accuracy was still controversial under certain combined stress states [5,21]. Recently, researchers from Imperial College London and KU Leuven initiated a project, called the Fiber Break Models for Designing novel composite microstructures and applications (FibreMoD), to further study the tensile response of UD laminates and benchmark the positive and negative points of several tensile failure criteria [22–25]. In terms of the *in situ* effects in failure predictions, the laminar transverse tensile and in-plane shear strengths were simply multiplied by specific coefficients in WWFE-II [18]. Nevertheless, this approximation was too aggressive for the outermost laminar where no constraint existed at the free side. This could lead to invalid failure predictions of multi-directional laminates. Herein, a general theoretical formulation for *in situ* strengths is demanded, with full consideration of the constraining effect of adjacent plies and the embedded laminar thickness.

From the literature review, it is seen that the progression on theoretical predictive models of damage and failure mechanisms for composites is clear from past researches, however, this has been scattered over numerous papers. Therefore, in the current study, the important development on the theoretical predictive models is firstly summarized and discussed. As reliable theoretical predictive models for composites under general loadings are still in the development stage, the other objective of the present investigation is to develop a physically-based failure analysis framework to predict the intralaminar failure onset and strengths for composite laminates under general stress states. Under multiaxial loading, interactive and coupling effects of stresses are carefully considered. The *in situ* strengths are introduced into the failure model using the simplified fracture mechanics-based approximation formula, with the constraining effects of both adjacent plies and embedded laminar thickness considered. A fiber kinking formulation is established with initial manufacturing defects considered for laminates used in practical engineering. To predict the strengths, a simplified degradation scheme of material properties is further proposed, differing various failure modes. Validations are then conducted on both unidirectional and multi-directional laminates subjected to uniaxial and multiaxial loads. Finally, relevant discussions and conclusions are drawn.

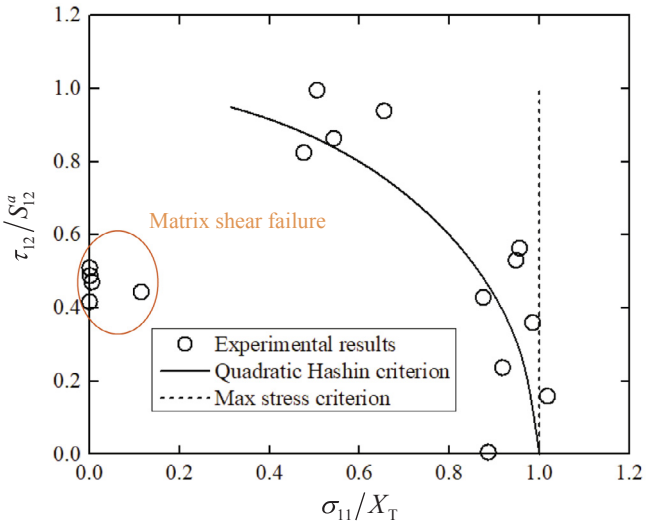

Fig. 1. Failure envelopes of $\sigma_{11} - \tau_{12}$ regarding different tension failure criteria with experimental data from the WWFE-I [27].

2. Longitudinal tension failure modeling

Under uniaxial tension, the simple maximum stress failure criterion is commonly used to predict the tensile strength of UD laminates. However, under complex loading, it is still controversial whether this criterion can accurately predict fiber rupture, since neither superposition nor coupling of stresses are included in the criterion [5,21,26]. Hashin [1,15] suggested that the shearing behavior in fiber tension failure should be carefully considered. With fiber tension failure assumed as the interaction of normal and shear stresses on the fracture surface, the quadratic superimposition formulation is proposed, as follows:

$$f_t = \left(\frac{\sigma_{11}}{X_T}\right)^2 + \left(\frac{\tau_{12}}{S_{12}^a}\right)^2 + \left(\frac{\tau_{13}}{S_{13}^a}\right)^2 = 1, \quad (\sigma_{11} \geqslant 0) \tag{1}$$

where $X_T$is the tensile strength in the fiber direction, $S_{12}^a$and S_{13}^a represent the axial shear strengths against fracture across the fibres due to pure shear stress, and f_t is the tensile failure factor.

Comparison of failure envelopes of the quadratic Hashin criterion and the maximum stress criterion is shown in Fig. 1. The experimental data were obtained from CFRP laminates (T300/BSL914C) under combined longitudinal tension and in-plane shearing from the WWFE-I [27]. The material properties are illustrated in Table 1. It can be seen that the quadratic criterion correlates well with data points for $\sigma_{11}/X_T > 0.5$, namely, the combined shearing and tension condition supporting an interaction of normal and shear stress. On the other hand, the simple maximum stress criterion can only give a good prediction for greater values of σ_{11}/X_T (near 1.0), namely, near pure tension. This indicates that the interaction of stresses needs to be carefully considered, and the quadratic criterion gives better predictions for multiaxial stress states. It is worth noting that data enclosed by an ellipse, shown in Fig. 1, represent the matrix shear failure and thus are excluded for the verification of the fiber rupture failure criterion.

Table 1
Mechanical properties of T300/BSL914C unidirectional laminates [27].

E_{11}	$E_{22} = E_{33}$	$G_{12} = G_{13}$	G_{23}	$\nu_{12} = \nu_{13}$	ν_{23}	β_{fr}^0/°
138 GPa	11 GPa	5.5 GPa	5.58 GPa	0.28	0.06	53
X_T	X_C	Y_T	Y_C	$S_{12} = S_{13}$	S_{23}	$S_{12}^a = S_{13}^a$
1500 MPa	900 MPa	27 MPa	200 MPa	80 MPa	70 MPa	130 MPa

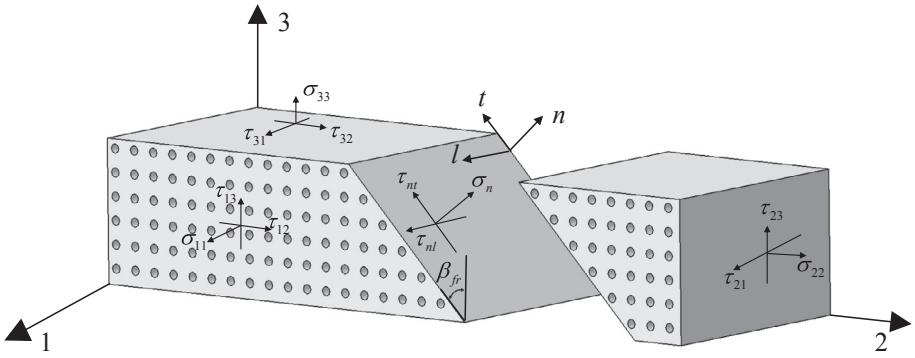

Fig. 2. Fracture plane of inter-fiber failure.

3. Inter-fiber failure modeling

On the basis of Mohr-Coulomb fracture theory and existing knowledge on damage mechanisms, Puck and co-authors [2,17] proposed the concept of fracture plane. In the case of brittle matrix fracture or inter-fiber failure (IFF) of laminates, a fracture plane parallel to the fiber direction is formed. It is assumed that normal and shear tractions acting on a fracture plane cause the failure. Fig. 2 illustrates the fracture plane and local coordinates as well as tractions acting on the plane. The angle between the fracture plane and thickness direction is defined as the fracture angle, β_{fr}. Regarding the stress states and fracture angle, the IFF is categorized into three different fracture modes as shown in Fig. 3. For normal tension or low level of compression interacting with shearing, the fracture plane is perpendicular to the loading direction with $\beta_{fr} = 0°$, namely, Mode A and B. This further supports Hashin's interaction formulations. For a higher level of transverse compression (Mode C), the fracture plane is inclined increasingly with the value of $|\sigma_{22}/\tau_{12}|$. Furthermore, it was noted in tests that fracture occurred in the inclined plane $\beta_{fr} = 57°$, instead of the plane where maximum shear stress was located ($\pm$ 45°), for CFRP unidirectional laminates under transverse compression [6,17]. This can be explained by the fact that the compressive stress and friction on the potential fracture plane cause the shift of the inclined angle. This phenomenon further consolidates the concept of fracture plane in Puck's failure criteria. The basic form for inter-fiber failure initiation in light of Puck's theory is given as follows:

$$\begin{aligned}&\text{IFFT: } \left(\frac{\sigma_n}{R_n^+}\right)^2 + \left(\frac{\tau_{nl}}{R_{nl} - p_{nl}\sigma_n}\right)^2 + \left(\frac{\tau_{nt}}{R_{nt} - p_{nt}\sigma_n}\right)^2 = 1,\ \sigma_n \geqslant 0\\ &\text{IFFC: } \left(\frac{\tau_{nl}}{R_{nl} - p_{nl}\sigma_n}\right)^2 + \left(\frac{\tau_{nt}}{R_{nt} - p_{nt}\sigma_n}\right)^2 = 1,\ \sigma_n < 0\end{aligned} \tag{2}$$

where σ_n, τ_{nl} and τ_{nt} are the tractions on the potential fracture plane as shown in Fig. 2, p_{nl} and p_{nt} are the inclination parameters of contour lines of the fracture body [28] that are used for representing the friction effects on the fracture plane, R_{nl} and R_{nt} are the in-plane and transverse fracture resistance of the fracture plane, while R_n^+ stands for the tension fracture resistance. IFFT and IFFC represent the inter-fiber tension and compression, respectively.

These tractions on the fracture plane appearing in Eq. (2) can be derived from stresses in material coordinates 1-2-3 using Eq. (3), as:

$$\begin{cases}\sigma_n = \sigma_{22}\cos^2\beta_{fr} + \sigma_{33}\sin^2\beta_{fr} + 2\tau_{23}\cos\beta_{fr}\sin\beta_{fr}\\ \tau_{nl} = \tau_{12}\cos\beta_{fr} + \tau_{13}\sin\beta_{fr}\\ \tau_{nt} = -\sigma_{22}\cos\beta_{fr}\sin\beta_{fr} + \sigma_{33}\cos\beta_{fr}\sin\beta_{fr} + \tau_{23}(\cos^2\beta_{fr} - \sin^2\beta_{fr})\end{cases} \tag{3}$$

Fracture resistance can be determined using material strength obtained at the corresponding single stress state. For uniaxial transverse tension ($\sigma_{22} > 0$) or pure in-plane shear (τ_{12}), the formed fracture plane is parallel to the principle material direction, so that the fracture angle is settled as $\beta_{fr} = 0°$ (only σ_{22} is applied) or $\beta_{fr} = 90°$ (only τ_{12} is applied). Therefore, R_n^+ and R_{nl} can be determined by transverse tension and in-plane shear strengths (Y_T and S_{12}), namely,

$$\begin{cases}R_n^+ = Y_T\\ R_{nl} = S_{12}\end{cases} \tag{4}$$

However, R_{nt} cannot be directly obtained. For a UD CFRP under the single stress of τ_{23}, the fracture angle is approximately 45° [29], not the same as the one where τ_{23} acts alone. Therefore, one cannot simply use the transverse shear strength S_{23} to represent the transverse fracture resistance R_{nt}. The inclined fracture plane indicates that the failure is caused by normal tension, which can additionally be derived from Eq. (3) with $\sigma_n > 0$. Given that shearing behavior contributes much more to the failure of UD laminates under transverse compression [2,29], uniaxial transverse compression can be used to determine R_{nt}.

For a single stress state $\sigma_{22} < 0$, the tractions on the fracture plane can be obtained using Eq. (3) where $\tau_{nl} = 0$. Then the IFF initiation criterion can be simplified as:

$$\tau_{nt} + p_{nt}\sigma_n = R_{nt},\ \sigma_n < 0 \tag{5}$$

Furthermore, the stress states of transverse compression (direction-2) failure on the fracture plane can be illustrated in the form of Mohr circle, with Eq. (5) represented by the failure envelope l_{fe} as shown in Fig. 4. The Mohr circle of pure transverse compression is tangent to the

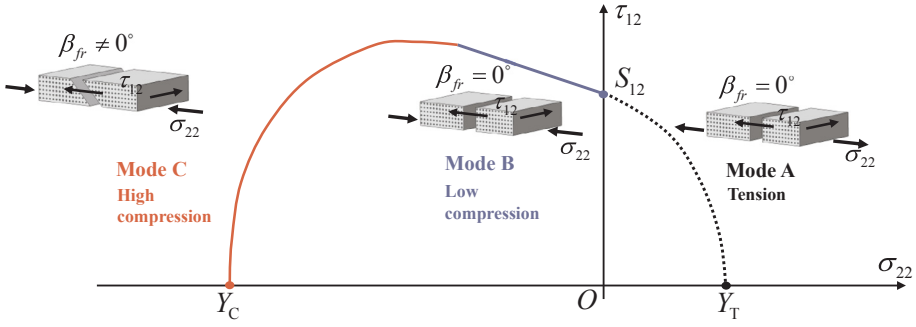

Fig. 3. Inter-fiber failure modes under combined transverse and shear stresses ($\sigma_{22} - \tau_{12}$).

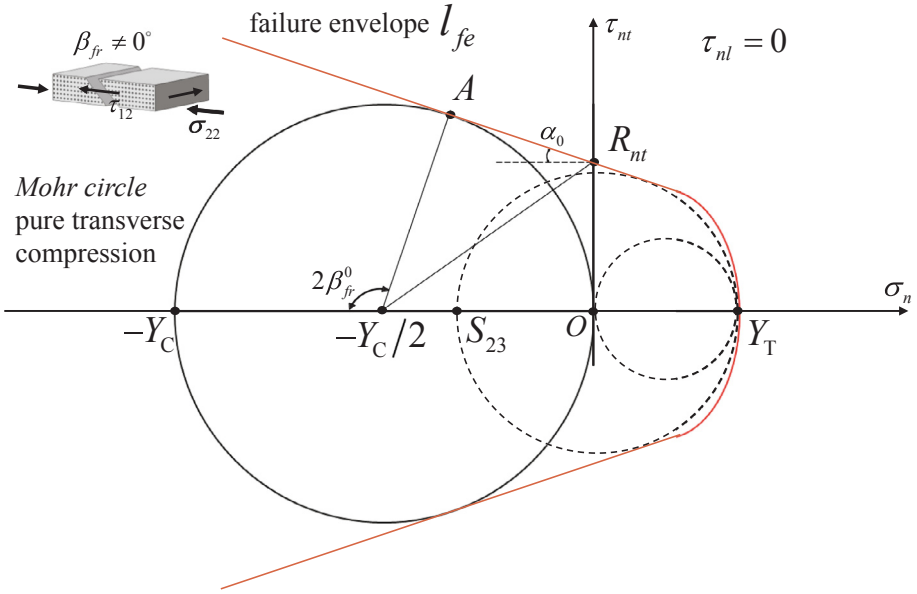

Fig. 4. Schematic illustration of Mohr circle for determining the fracture resistance R_{nt} in linear inter-fiber failure criteria.

failure envelope l_{fe} at point **A** where the stress state satisfies the failure initiation criterion. This reveals the relationship between the inclination parameter p_{nt} and the fracture angle β^0_{fr}, which is

$$p_{nt} = -\tan\alpha_0 = -\cot 2\beta^0_{fr} \tag{6}$$

Along with stress states at point **A**, submitting Eqs. (3) and (6) into Eq. (5), one can derive R_{nt} as follows:

$$Y_C \cos\beta^0_{fr} \sin\beta^0_{fr} + Y_C \cot 2\beta^0_{fr} \cos^2\beta^0_{fr} = R_{nt} \Rightarrow R_{nt} = 2Y_C \cot\beta^0_{fr} \tag{7}$$

And p_{nl} is simply estimated using Eq. (8), as

$$p_{nl} = \frac{R_{nl}}{R_{nt}} p_{nt} \tag{8}$$

Further investigations show that the predicted strengths using the basic form (Eq. (5)) is generally greater than experimental data especially when high compression traction ($\sigma_n < 0$) acts on the potential fracture plane. Corrections are made by Puck and co-authors [17], namely,

$$\text{IFFT: } \sqrt{\left[\left(\frac{1}{R^{At}_{\perp}} - \frac{p^t_{\perp\psi}}{R^A_{\perp\psi}}\right)\sigma_n\right]^2 + \left(\frac{\tau_{nt}}{R^A_{\perp\perp}}\right)^2 + \left(\frac{\tau_{nl}}{R^A_{\parallel\perp}}\right)^2} + \frac{p^t_{\perp\psi}}{R^A_{\perp\psi}}\sigma_n = 1 \quad , \sigma_n \geqslant 0$$

$$\text{IFFC: } \sqrt{\left(\frac{p^c_{\perp\psi}}{R^A_{\perp\psi}}\sigma_n\right)^2 + \left(\frac{\tau_{nt}}{R^A_{\perp\perp}}\right)^2 + \left(\frac{\tau_{nl}}{R^A_{\parallel\perp}}\right)^2} + \frac{p^c_{\perp\psi}}{R^A_{\perp\psi}}\sigma_n = 1 \quad , \sigma_n < 0 \tag{9}$$

The main difference between the two formulations lies in the description of the Mohr-Coulomb fracture behavior. In Eq. (5), the effective shear fracture resistance ($R_{nl} - p_{nl}\sigma_n$, $R_{nt} - p_{nt}\sigma_n$) increases linearly with the normal traction σ_n while parabolic relation is represented in Eq. (9). Fig. 5 illustrates the Mohr circle to determine the fracture parameters in the parabolic form. Therefore, the fracture resistance parameters can be derived in an analogous way as the case of the linear failure criteria presented above, as:

$$R^A_{\perp\perp} = \frac{Y_C}{2(1 + p^c_{\perp\perp})}, \tag{10}$$

$$R^{At}_{\perp} = Y_T, \tag{11}$$

$$R^A_{\perp\parallel} = S_{12}, \tag{12}$$

$$R^A_{\perp\psi} = \left(\frac{\cos\psi}{R^A_{\perp\perp}}\right)^2 + \left(\frac{\sin\psi}{R^A_{\perp\parallel}}\right)^2 \tag{13}$$

The inclination parameters are determined using the following equations:

$$\frac{p^i_{\perp\psi}}{R^A_{\perp\psi}} = \frac{p^i_{\perp\perp}}{R^A_{\perp\perp}}\cos^2\psi + \frac{p^i_{\perp\parallel}}{R^A_{\perp\parallel}}\sin^2\psi, \quad i = t, c \tag{14}$$

$$\cos^2\psi = \frac{\tau^2_{nt}}{\tau^2_{nt} + \tau^2_{nl}}, \quad \sin^2\psi = \frac{\tau^2_{nl}}{\tau^2_{nt} + \tau^2_{nl}} \tag{15}$$

For typical brittle CFRP/epoxy and GFRP/epoxy UD laminates, the values of inclination parameters are recommended as listed in Table 2. Recently, Gu and Chen [30] pointed out that the inclination parameters slightly varied from brittle to ductile materials. In their extended models of Puck's theory, the predictions were in good agreement with experimental data particularly for UD composite laminates with high Y_C/Y_Tratios. As the difference between the parabolic and extended models is quite small, the parabolic model is preferred in this work while the inclination parameters are slightly updated according to the results in [30].

3.1. *In situ* strength effect

The *in situ* strength effect refers to the fact that the strengths of a single laminar embedded in multi-directional laminates are higher than those of unidirectional laminates obtained by classic material tests. This is because crack initiation and propagation in a single laminar are delayed by adjacent plies with different properties like ply thickness or ply angles. Existing results show that the *in situ* effect should be carefully taken into account, especially for transverse tension and in-plane shear strengths [31–34].

With novel experimental design and data reduction techniques, the mechanism of *in situ* strength effect has been well studied and explained with more experimental data and observations revealed [35–37]. A variety of theoretical analysis models have been proposed to quantify the effects, which were subsequently applied in numerical studies to predict the *in situ* [6,9,38–40].

Chang and Lessard [33] introduced an empirical formula for calculating the *in situ* transverse tension and in-plane shear strengths with several fitting parameters obtained using the reverse method. With

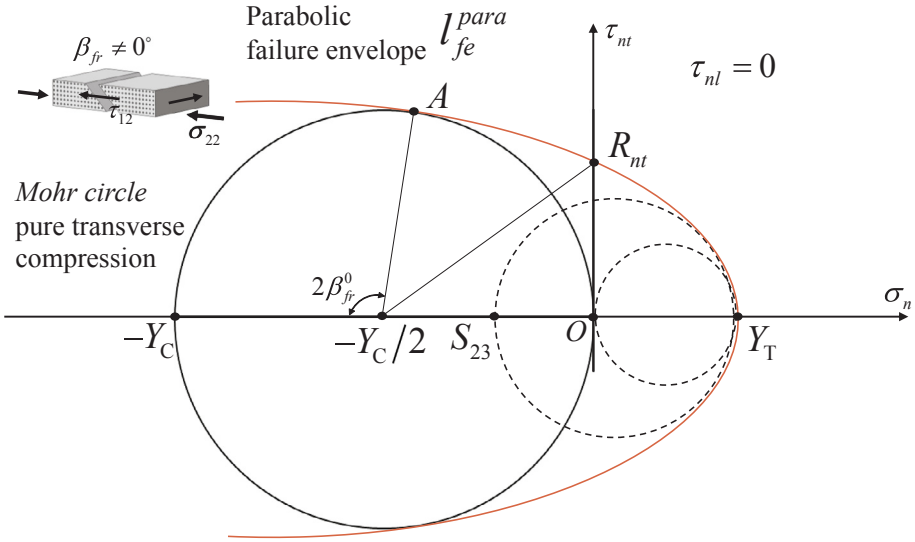

Fig. 5. The schematic illustration of Mohr circle for determining the fracture resistance R_{nt} in parabolic inter-fiber failure criteria.

Table 2
Inclination parameters of CFRP/epoxy UD laminates [17,28,30].

Material system	$p_{\perp\perp}^{t}$	$p_{\perp\perp}^{c}$	$p_{\perp\parallel}^{t}$	$p_{\perp\parallel}^{c}$
CFRP/epoxy	0.25–0.325	0.25–0.325	0.35	0.3
GFRP/epoxy	0.20–0.25	0.20–0.25	0.3	0.25

amounts of experimental data on specific material systems and layups, simple multiple values of the corresponding strengths have been recommended to represent *in situ* strengths [41,42]. Wang and Karihaloo [34,35] advanced a general theoretical solution for *in situ* strengths based on fracture mechanics, with full consideration on the constraining effect of adjacent plies. Recently, Dong et al. [39] promoted the solution to more CFRP laminates for further validating its feasibility and reliability. Camanho et al. [9] studied the influence of embedded laminar thickness and extended the original solution. For both accuracy and simplicity, the *in situ* strengths in this work are calculated using the solution proposed by [39], given by:

$$\begin{cases} Y_T^{is} = Y_T\left[1 + \frac{A}{N^B} f_t(\Delta\theta)\right] \\ S_{12}^{is} = S_{12}\left[1 + \frac{C}{N^D} f_s(\Delta\theta)\right] \end{cases} \tag{16}$$

where Y_T^{is} and $S_{12}^{is}$are the *in situ* transverse tension and in-plane shear strengths, and {*A, B, C, D*} are fitting parameters determined by the layups. Wang and Karihaloo [34] discussed the most applied layups and the likely values of {*A, B, C, D*}. The values {1.7, 3.4 4.0 1.0} were recommended when experimental data were absent. *N* is the number of plies in the calculated unidirectional laminar, representing the size effect of the thickness. $f_t(\Delta\theta)$ and $f_s(\Delta\theta)$denote the constraining effects of adjacent plies, which are determined as:

$$\begin{cases} f_t(\Delta\theta) = \min\left[\frac{\sin^2(\Delta\theta_u)}{1+\sin^2(\Delta\theta_u)}, \frac{\sin^2(\Delta\theta_d)}{1+\sin^2(\Delta\theta_d)}\right] \\ f_s(\Delta\theta) = \min\left[\frac{\sin^2(2\Delta\theta_u)}{1+\sin^2(2\Delta\theta_u)}, \frac{\sin^2(2\Delta\theta_d)}{1+\sin^2(2\Delta\theta_d)}\right] \end{cases} \tag{17}$$

where $\Delta\theta_i (i = u, d)$is the ply angle difference between the calculated laminar and the very neighboring upper or lower one.

3.2. Determination of fracture angle

From Eqs. (3) and (9), the failure is determined by the fracture angle in addition to the stress states. Mathematically, the maximum value of the left part of Eq. (9) corresponds to the potential fracture plane and angle, given by:

$$f_{IFF}(\beta_{fr}) = \max[f_{IFF}(\sigma_{22}, \sigma_{33}, \tau_{12}, \tau_{13}, \tau_{23}, \beta)], (\beta \in [-90°, 90°]) \tag{18}$$

where $f_{IFF}$is the failure index representing the left part of Eq. (9).

Enumeration algorithm was firstly introduced to determine β_{fr}[2,17]. This leads to testing all the angles individually at an interval of 1°, with a high computational effort. To reduce testing points, Davila et al. [7] and Pinho et al. [6] estimated the potential fracture angle using trial angles and drawing trial failure envelopes. Golden section search algorithm (GSSA) was further introduced and extended to significantly improve the computational efficiency [29,43,44].

In GSSA, one unknown point is generated by two known points, with the distance satisfying the golden section rule as schematically illustrated in Fig. 6. For a stress state, $(\beta_1, f_{IFF}(\beta_1))$ and $(\beta_2, f_{IFF}(\beta_2))$ are two preset points, then two new points (β_3, β_4) can be determined as:

$$\frac{\beta_2 - \beta_3}{\beta_3 - \beta_1} = \frac{1+\sqrt{5}}{2}, \frac{\beta_2 - \beta_4}{\beta_4 - \beta_3} = \frac{1+\sqrt{5}}{2} \tag{19}$$

In case $f_{IFF}(\beta_3) > f_{IFF}(\beta_4)$, the new search sub-range is located at $[\beta_2, \beta_3]$, otherwise $[\beta_1, \beta_4]$. After several search trials, a parabola can be constructed as the target function to reduce iterations and searching time [29], yielding

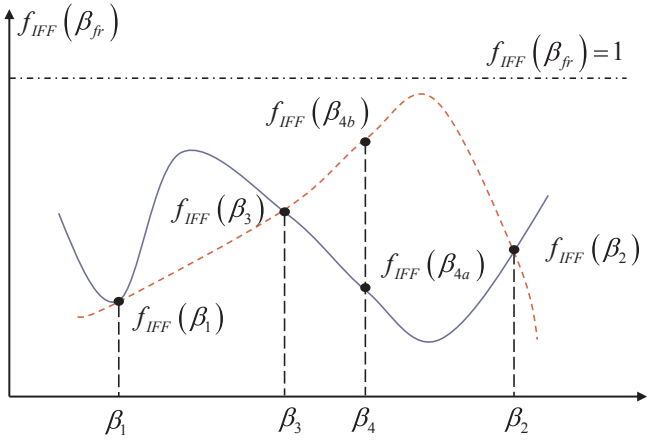

Fig. 6. Schematic golden section search algorithm.

$$F(\beta) = f_{IFF}(\beta_a)\frac{(\beta-\beta_b)(\beta-\beta_c)}{(\beta_a-\beta_b)(\beta_a-\beta_c)} + f_{IFF}(\beta_b)\frac{(\beta-\beta_a)(\beta-\beta_c)}{(\beta_b-\beta_a)(\beta_b-\beta_c)} + f_{IFF}(\beta_c)\frac{(\beta-\beta_a)(\beta-\beta_b)}{(\beta_c-\beta_a)(\beta_c-\beta_b)} \tag{20}$$

where $[\beta_a, \beta_b]$ is the sub-range after several trials and $\beta_c$is the golden section point. By searching the maximum of Eq. (20), the potential fracture angle β_{fr} can be determined, as:

$$\beta_{fr} \approx \beta_b - \frac{1}{2} \times \frac{(\beta_b-\beta_a)^2(f_{IFF}(\beta_b)-f_{IFF}(\beta_c)) - (\beta_b-\beta_c)^2(f_{IFF}(\beta_b)-f_{IFF}(\beta_a))}{((\beta_b-\beta_a)(f_{IFF}(\beta_b)-f_{IFF}(\beta_c)) - (\beta_b-\beta_c)(f_{IFF}(\beta_b)-f_{IFF}(\beta_a)))} \tag{21}$$

4. Longitudinal compression failure modeling

Compressive loading on aeronautical composites structures usually leads to kinking failure and matrix splitting within the kink bands, especially for CFRP and GFRP laminates with thin fibers and high fiber volume fractions (40%-60%) [45]. Rosen [46] firstly proposed the kinking strength model based on fiber micro-buckling. However, the model provided the upper limit of compression strengths, with predictions 2–4 times larger than experimental results. Argon [47] then considered matrix shear strength along with fiber misalignment in the kinking model. Schultheisz and Waas [8] concluded from amounts of experimental data that localized micro-defects (e.g. fiber misalignment and matrix cracking) mostly contributed to the formation of kink bands. Subsequently, 2D and 3D kinking models were proposed based on different failure criteria [6,7,12,48]. In this work, the kinking model is established on the basis of Argon's approach [47] and successive developments by Davila et al. [7] and Pinho et al. [6].

4.1. Fiber kinking model

Fiber misalignment and localized matrix failure lead to the formation of kinking bands. It is of great significance to obtain tractions on the fracture plane similar to those of inter-fiber failure. Different coordinate systems used in the proposed fiber kinking model are illustrated in Fig. 7. $1-2-3$ is the material coordinate system where axis-1 denotes fiber direction, with axis-2 and axis-3 representing the transverse and thickness directions as shown in Fig. 7(a). The coordinate system of kinking plane is denoted by $k_1-k_2-k_3$. It is transformed by rotating $1-2-3$ around axis-1 with an angle φ. Fig. 7(b) schematically illustrates fiber misalignment in the kinking plane with the kinking angle θ. $m_1-m_2-m_3$ is the local misalignment coordinate system of kinking fibers. Similarly, $m_1-m_2-m_3$ is obtained by rotating $k_1-k_2-k_3$ around axis-k_3 with kinking angle θ. The local matrix fracture plane is demonstrated in Fig. 7(c) where the fracture angle is denoted by $\alpha_{fr}^{\text{kink}}$. The transformation of stresses is as follows:

$$\sigma^k = \mathbf{R}^k(\varphi)\sigma^f[\mathbf{R}^k(\varphi)]^{\mathbf{T}},\ \sigma^m = \mathbf{R}^m(\theta)\sigma^k[\mathbf{R}^m(\theta)]^{\mathbf{T}} \tag{22}$$

where $\mathbf{R}^k(\varphi)$ and $\mathbf{R}^m(\theta)$ are the transformation matrices defined as:

$$\mathbf{R}^k(\varphi) = \begin{bmatrix} 1 & 0 & 0 \\ 0 & \cos\varphi & \sin\varphi \\ 0 & -\sin\varphi & \cos\varphi \end{bmatrix},\quad \mathbf{R}^m(\theta) = \begin{bmatrix} \cos\theta & \sin\theta & 0 \\ -\sin\theta & \cos\theta & 0 \\ 0 & 0 & 1 \end{bmatrix} \tag{23}$$

Hence, stresses at $1-2-3$ system can be projected into $m_1-m_2-m_3$ and further onto the matrix fracture plane, which gives

$$\begin{cases} \sigma_n^{kink} = \sigma_{22}^m\cos^2\alpha_{fr} + \sigma_{33}^m\sin^2\alpha_{fr} + 2\tau_{23}^m\cos\alpha_{fr}\sin\alpha_{fr} \\ \tau_{nl}^{kink} = \tau_{12}^m\cos\alpha_{fr} + \tau_{13}^m\sin\alpha_{fr} \\ \tau_{nt}^{kink} = -\sigma_{22}^m\cos\alpha_{fr}\sin\alpha_{fr} + \sigma_{33}^m\cos\alpha_{fr}\sin\alpha_{fr} + \tau_{23}^m(\cos^2\alpha_{fr} - \sin^2\alpha_{fr}) \end{cases} \tag{24}$$

Then the local matrix failure is determined using inter-fiber failure criteria with applied kinking stresses, as:

$$\begin{aligned} &\sqrt{\left[\left(\frac{1}{R_\perp^{At}} - \frac{p_{\perp\psi}^t}{R_{\perp\psi}^A}\right)\sigma_n^{kink}\right]^2 + \left(\frac{\tau_{nt}^{kink}}{R_{\perp\perp}^A}\right)^2 + \left(\frac{\tau_{nl}^{kink}}{R_{\parallel\perp}^A}\right)^2} + \frac{p_{\perp\psi}^t}{R_{\perp\psi}^A}\sigma_n^{kink} = 1,\ \sigma_n^{kink} \geqslant 0 \\ &\sqrt{\left(\frac{p_{\perp\psi}^c}{R_{\perp\psi}^A}\sigma_n^{kink}\right)^2 + \left(\frac{\tau_{nt}^{kink}}{R_{\perp\perp}^A}\right)^2 + \left(\frac{\tau_{nl}^{kink}}{R_{\parallel\perp}^A}\right)^2} + \frac{p_{\perp\psi}^c}{R_{\perp\psi}^A}\sigma_n^{kink} = 1,\ \sigma_n^{kink} < 0 \end{aligned} \tag{25}$$

4.2. Solution for kinking band parameters

From the formulation of fiber kinking model, the determination of angle parameters (ϕ, θ) is crucial to predict the longitudinal compression failure.

During the crack formation, fiber defects result in shear stiffness decreasing in the kink bands.The out-of-plane shear stress (τ_{23}^k) on the kinking plane is assumed to be zero. In fact, if $\tau_{23}^k \neq 0$, fibers would keep deflecting perpendicular to the kinking plane, contradicting the current configuration [6]. From Eq. (23), the kinking plane angle φ can be derived as,

$$\varphi = \frac{1}{2}\arctan\left(\frac{2\tau_{23}^f}{\sigma_{22}^f - \sigma_{33}^f}\right) \tag{26}$$

Relation between fiber misalignment angle (θ) and shear strain in the local misalignment plane (γ_{12}^m) is shown in Fig. 8, as:

$$\theta = \frac{\tau_{12}^m}{|\tau_{12}^m|}(\gamma_{12}^m + \theta_0) \tag{27}$$

where $\tau_{12}^m/|\tau_{12}^m|$ denotes the consideration on directions of initial misalignment angle, namely, $\pm\theta_0$. γ_{12}^m can be determined by the shear strain-stress constitutive relationship, which can be briefly expressed as:

$$\tau_{12}^m = f(\gamma_{12}^m) \tag{28}$$

Therefore, at a general 3D stress state, combining the off-axis stress transformation in Eq. (23), gives,

$$f(\gamma_{12}^m) = -\sin(\theta)\cos(\theta)(\sigma_{11}^k - \sigma_{22}^k) + (\cos^2(\theta) - \sin^2(\theta))|\tau_{12}^k| \tag{29}$$

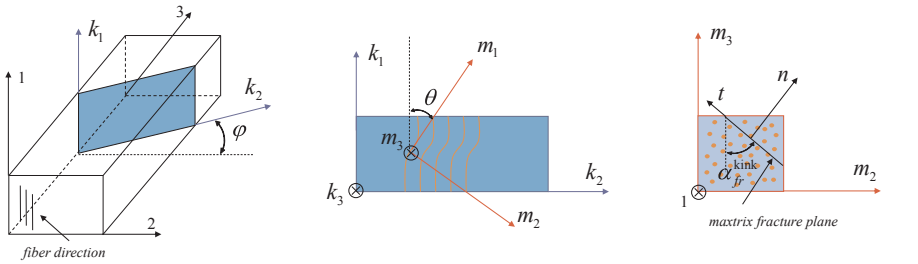

(a) Material coordinates (b) Kinking plane coordinates (c) Fiber misalignment coordinates

Fig. 7. Schematic illustration of coordinates in the kinking band.

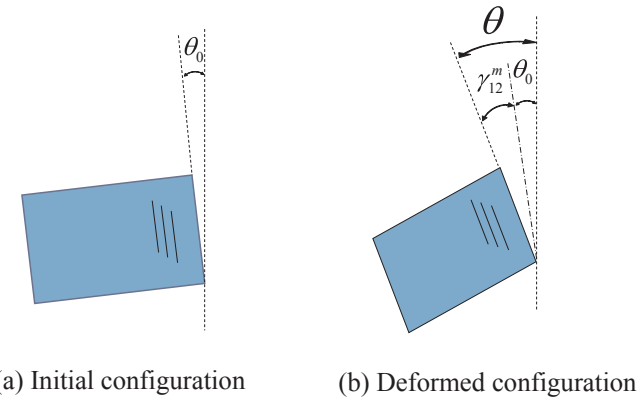

Fig. 8. Relation between the fiber misalignment angle and shear strain.

For sufficiently small values of θ, Eq. (29) can be approximated as,

$$f(\gamma_{12}^m) \approx -(\sigma_{11}^k - \sigma_{22}^k)\theta + |\tau_{12}^k| \tag{30}$$

Specifically, for linear shear response, shear strain in the local misalignment plane γ_{12}^m can be simplified as,

$$\gamma_{12}^m = \frac{\theta_0 G_{12} + |\tau_{12}^k|}{G_{12} + \sigma_{11}^k - \sigma_{22}^k} - \theta_0 \tag{31}$$

On the other hand, with nonlinear shear response taken into account, the Newton-Raphson iteration method is applied to solve Eq. (30) with the additional mathematical condition, as:

$$\frac{\partial f(\gamma_{12}^m)}{\partial \gamma_{12}^m} = -(\sigma_{11}^k - \sigma_{22}^k)\cos 2\theta - 2\,|\tau_{12}^k|\,\sin 2\theta \tag{32}$$

5. Degradation scheme of material properties

At a stress state, in case that one of the failure criteria is satisfied as stated in previous sections, the corresponding material property is supposed to be degraded in order to characterize the decrease of structural load bearing capacity. The left hand terms of Eqs. (1), (9), (25) are denoted as f_i, $(i = t, IFFT, IFFC, kink)$. The degradation differs for different failure modes and is listed below.

(1) Fiber tension failure. The failure caused by fiber breakage is generally instantaneous and catastrophic, leading to massive loss in load bearing capacity. Therefore, when fiber tension failure is triggered, all the in-plane mechanical properties are simply degraded to zero, i.e.,

$$\{E_{11}, E_{22}, G_{12}, \nu_{12}\}_{ft} \rightarrow \{0, 0, 0, 0\}. \tag{33}$$

(2) Inter-fiber failures. In case that the normal traction on the fracture plane is non-negative ($\sigma_n \geq 0$), inter-fiber tensile failure (IFFT) occurs. The fracture plane is usually perpendicular to the loading direction, causing an crack to remain open. It leads to a certain degradation in the transverse elastic and in-plane shear modulus as well as the Poisson's ratio, expressed as:

$$\{E_{22}, G_{12}, \nu_{12}\}_{IFFT} \rightarrow \{\eta_{IFFT}E_{22}, \eta_{IFFT}G_{12}, \eta_{IFFT}\nu_{12}\}. \tag{34}$$

On the other hand, for inter-fiber compression failure (IFFC), the fracture plane remains close with a sliding tendency. As the compressive load increases, the closed crack surface still has the capability to transmit lateral compressive loads through crack contact. Hence, only the shear elastic modulus is degraded as demonstrated in Eq. (35),

$$\{E_{22}, G_{12}, \nu_{12}\}_{IFFC} \rightarrow \{E_{22}, \eta_{IFFC}G_{12}, \nu_{12}\}. \tag{35}$$

where η_{IFFi}, $i = (T, C)$ are the degradation index of the inter-fiber failure. The initial value of η_{IFFi} is set as 1.0 indicating no damage. When the failure criterion is triggered, η_{IFFi} is assigned to a value between 0.0 and 1.0.

(3) Fiber kinking failure. In case that kink bands are formed, the corresponding laminar can hardly carry any load since amounts of fiber misalignments and localized matrix failures exist in the kink bands. Therefore, all the in-plane mechanical properties are simply degraded to zero, namely,

$$\{E_{11}, E_{22}, G_{12}, \nu_{12}\}_{ft} \rightarrow \{0, 0, 0, 0\}. \tag{36}$$

From the physical significance of failure envelopes, a laminar should be ensured to remain at the critical status after property degradation. In other words, the failure factors should stay at one in case of failure criteria satisfied, namely, $f_i = 1.0$. This further indicates that the degradation indexes (η_i) of different failure modes should be defined as functions of the corresponding f_i. However, in numerical iterations of failure analysis, an increase of stresses may result in higher values of the left hand terms in failure criteria. To distinguish from the physical definition of failure factors, the values of the left hand terms in the failure criteria are denoted as the trial stress factors $f_{E,i}$. Corresponding stresses in the current configuration are trial stresses. Furthermore, the function of η_i and $f_{E,i}$ defined in [2] is introduced in this work to characterize the failure process, as:

$$\eta_i = 1/f_{E,i}(i = IFFT, IFFC), \quad f_E \geqslant 1 \tag{37}$$

6. Verification and discussion

Fig. 9 presents the predicted $\sigma_{22} - \tau_{12}$ failure envelopes of glass- and carbon-fiber reinforced unidirectional (UD) laminates, namely, E-Glass/LY556 [27], AS4/55A [49], T800/3900 [50] and AS4/3501 [51]. The material properties are listed in Table 3. It is observed that the present predictions correlates well with existing experimental data.

Both the experimental data and theoretical predictions show that the maximum shear stress τ_{12}increases with increasing $|\sigma_{22}|$ at low level of transverse compression. This indicates that transverse compression can inhibit shearing damage to a certain extent. In this case, in-plane shear failure occurs mainly in UD laminates with the fracture angle located between 0° and 40° [7]. For higher transverse compression ($|\sigma_{22}| > 0.7X_C$), shearing effect is less on the failure, and the UD

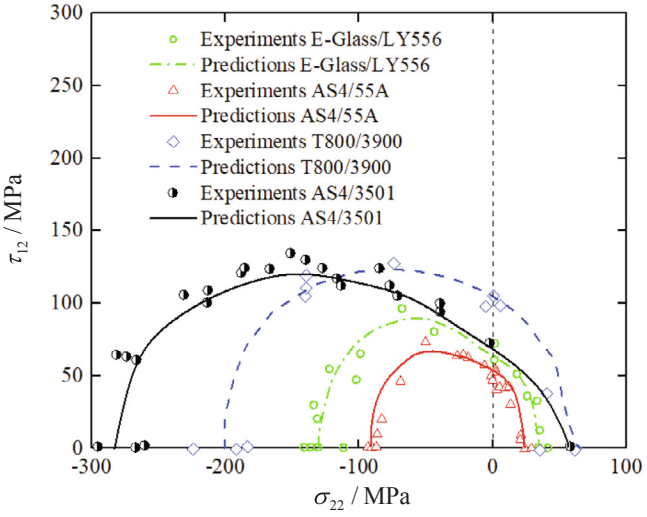

Fig. 9. $\sigma_{22} - \tau_{12}$ failure envelopes of unidirectional laminates made of different composite materials.

Table 3
Material properties of investigated composites in terms of $\sigma_{22} - \tau_{12}$ failure envelopes [49,27,50,51].

	E-Glass/LY556	AS4/55A	T800/3900	AS4/3501
E_{11}/GPa	54	120	175	126
E_{22}/GPa	18	12	10	11
ν_{12}	0.28	0.28	0.30	0.28
G_{12}/GPa	5.8	6.5	5.2	6.6
X_T/MPa	1140	1950	2000	2323
X_C/MPa	570	1480	1500	1200
Y_T/MPa	35	50	60	60
Y_C/MPa	114	200	201	200
S_{12}/MPa	72	79	100	74
β^0_{fr}/°	53	53	53	53

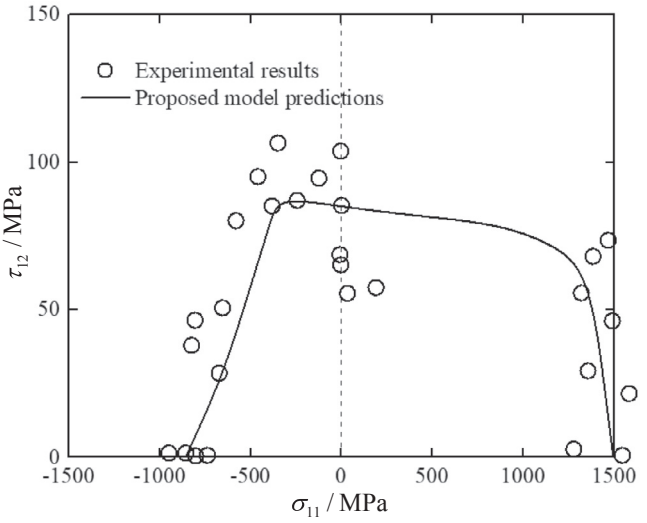

Fig. 10. $\sigma_{11} - \tau_{12}$ failure envelope of T300/BLS914C unidirectional laminates.

laminates fail mostly in compressive behavior. The proposed model captures this phenomenon, further validating its feasibility.

Hinton et al. [27] reported experimental data of T300/BLS914C UD laminates under combined loading status $\sigma_{11} - \tau_{12}$. The mechanical properties T300/BLS914C are listed in Table 1.

Fig. 10 shows a good agreement between the predicted failure envelope and experimental data points. It should be mentioned that in-plane shear nonlinearity is taken into account by using the cubic spline interpolation function [52]. In the case of high level tension ($\sigma_{11} \geq 1000$ MPa), shearing behavior has less influence on fracture mode. The quadratic Hashin criterion provides well-fitted predictions, with test data points distributed around both sides of the failure envelope. Similar to transverse compression, for low levels of $|\sigma_{11}|$ (e.g. -400 MPa $< \sigma_{11} < 0$ MPa), fiber compression slightly enhances the shear fracture resistance. Both the predictions and test data capture this phenomenon as shown in Fig. 10. This finding may be further applied to prestressed composite structures in engineering applications. Regarding the pure shearing state ($\sigma_{11} = 0$), it is noted that a high dispersion of data points is observed in Fig. 10. It has been suggested that experimental errors caused the higher values of some data in comparison to the shear strength [3,12]. For this consideration, no special emphasis is given in this study. Accordingly, it can be concluded that the proposed model can give a satisfactory prediction of the combined $\sigma_{11} - \tau_{12}$ failure.

The predicted bi-axial $\sigma_{11} - \sigma_{22}$ failure envelope of E-Glass/MY750 UD laminates is illustrated in Fig. 11. Experimental data were employed in WWFE [3,27]. Relevant mechanical properties of E-Glass/MY750 can be found in Table 4.

As can be noted in Fig. 11, the four interaction points of the failure

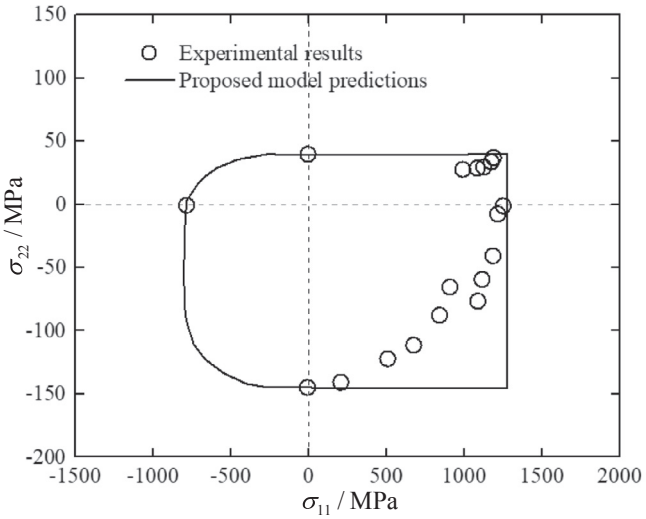

Fig. 11. $\sigma_{11} - \sigma_{22}$ failure envelope of E-Glass/MY750 unidirectional laminates.

Table 4
Mechanical properties of E-Glass/MY750 unidirectional laminates [16].

E_{11}	E_{22}	G_{12}	ν_{12}	β^0_{fr}
46 GPa	16 GPa	5.83 GPa	0.28	53°
X_T	X_C	Y_T	Y_C	S_{12}
1280 MPa	800 MPa	40 Mpa	145 MPa	73 MPa

envelope and $\sigma_{11} - \sigma_{22}$) axes exactly correspond to the four basic strengths X_T, X_C, Y_T, Y_C obtained from tests. In the fourth quadrant, however, the test data are more conservative than the predictions. This may be attributed to the fact of that experimental data were obtained by ± 5° rather than 0° UD laminates. In the second and third quadrants, the failure envelope shows that longitudinal compression slightly reduces the transverse tension and compression resistance, though few test data were obtained from the combined loading. On the other hand, the predictions fit well with experimental results in the first quadrant in bi-axial tension. To further examine the proposed model, more tests should be performed in the future.

Soden et al. [16] presented several experimental tests of multi-directional composite laminates under uniaxial and biaxial loads in WWFE. Some of experimental results are employed in this work to further validate the proposed model as shown in Figs. 12 and 13.

Fig. 12 displays the strain-stress responses of orthogonal E-Glass/MY750 laminates ($[0/90]_s$) under uniaxial tension. Predictions with and without considering*in situ* strengths are both demonstrated. In general, a good agreement of the strain-stress curves is observed between the prediction and test data, regardless of the consideration of *in situ* strengths. And both predictions capture initial failure in the 90° layer, indicating that *in situ* effects have little influence on the loading path. However, the initial failure stress predicted by the model without *in situ* strengths is only 80 MPa, which is notably lower than the test result (159 MPa). With the *in situ* strength accounted for, the predicted initial failure stress is 150 MPa, correlating well with the test result as shown in Fig. 12 and Table 5.

In the case of biaxial tension ($\sigma_x - \sigma_y$), the strain-stress responses for quasi-isotropic AS4/3501 laminates ($[90/\pm45/0]_s$) are illustrated in Fig. 13. Similarly, compared to that using the basic strengths, the initial failure stress predicted using the *in situ* strengths is closer to the test result, with a deviation of 8.8% as is seen in Table 5. This proves the importance of considering *in situ* strengths in failure analysis. The consistency of the predicted strain-stress responses with experimental data points after initial failure further validates the feasibility of the

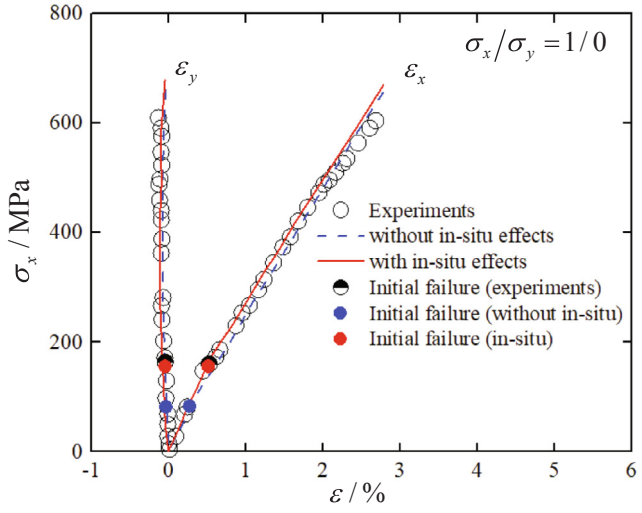

Fig. 12. Strain-stress responses of $[0/90]_s$ E-Glass/MY750 laminates under uniaxial tension.

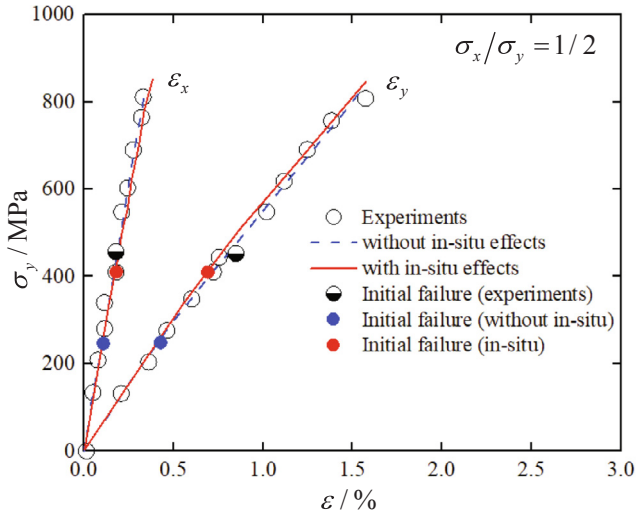

Fig. 13. Strain-stress responses of $[90/\pm45/0]_s$ AS4/3501 laminates under combined $\sigma_x - \sigma_y$.

proposed material degradation scheme.

Fig. 14 illustrates both the initial and final failure envelopes of a angle-ply laminate ($[\pm55]_s$), with experimental data taken from [16]. A good agreement is observed between the predicted final failure envelope and experimental data, indicating once again the reliability of the proposed failure model. It is noted that the angle-ply laminate is easier to fail under biaxial tension and compression ($\sigma_x/\sigma_y < 0$), compared to its uniaxial strengths as shown in the second and fourth quadrants of Fig. 14. On the other hand, both the predictions and experimental data in the first and third quadrants show that biaxial tension and biaxial compression enhance both the uniaxial tension and compression fracture resistance of the angle-ply laminate.

Particularly for biaxial compression in the third quadrant, the predicted failure envelope provides conservative results relative to some of

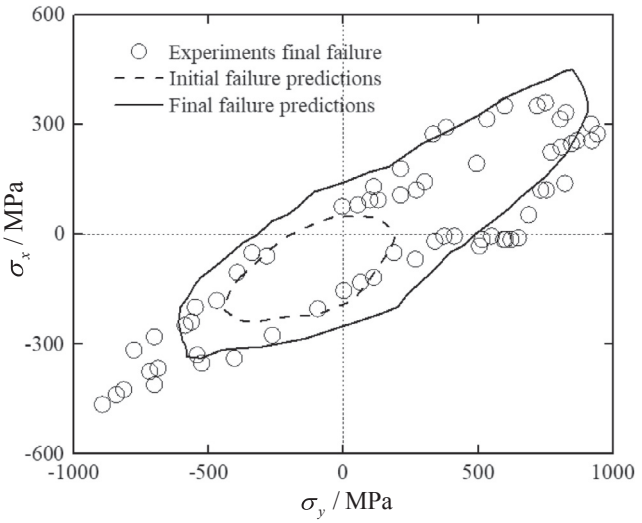

Fig. 14. Failure envelopes of $[\pm55]_s$ E-Glass/MY750 laminates under combined $\sigma_x - \sigma_y$.

the test data (e.g. $\sigma_x < -300$ MPa). This might be the result of that the fiber volume fraction of biaxial compression specimens (68%) was not consistent with that of biaxial tension ones (60%) in tests [3]. And the material properties used in the present failure model are based on those of unidirectional laminates with the fiber volume fraction fixed at 60% in accordance with the literature [16].

7. Conclusions

In this work, a physically-based failure analysis framework is proposed to predict the intralaminar failure and strengths for composite laminates, including fiber tension, inter-fiber failure (IFF) and fiber kinking failure. In 3D stress states, superposition and coupling effects are carefully considered for multiaxial loads. The *in situ* strengths are introduced into the failure model using fracture mechanics-based approximation formula. The size effect of embedded laminar thickness and the constraining effects of adjacent plies are taken into account simultaneously. For CFRP and GFRP laminates with thin fibers and high fiber volume fractions (40%-60%), a longitudinal fiber kinking model is established with initial manufacturing defects considered. To characterize the decrease of load bearing capacity and final failure, a simplified degradation scheme of material properties is proposed, differing from different failure modes.

Predicted failure envelopes of various laminates under multiaxial loads are illustrated, like unidirectional (UD), orthogonal, quasi-isotropic and angle-ply laminates. Good agreement is observed comparing the predicted initial and final failure envelopes with experimental data. From both experimental data and predictions, it is further found that slight compression could enhance the in-plane shear fracture resistance of UD laminates, whereas biaxial tension and biaxial compression enhance the uniaxial tension and compression strengths of angle-ply laminates.

The influence of *in situ* strengths on initial failure stress and strain-stress responses is discussed in detail. Results show that predictions obtained using basic strengths considerably underestimated the initial

Table 5
In situ effects on initial failure stresses.

	Experiments	without *in situ* effects	with *in situ* effects
$[0/90]_s$ E-Glass/MY750	159 MPa	80 MPa (−49.6%)	150 MPa (−5.6%)
$[90/\pm45/0]_s$ AS4/3501	439 MPa	260 MPa (−40.7%)	400 MPa (−8.8 %)

failure stress while the model with *in situ* effects considered give a good agreement with test data. Strain-stress responses are well captured and consistent with experimental data. This further validates the feasibility of the proposed material degradation scheme. On the other hand, Like most failure theories for fiber-reinforced composite laminates, this proposed framework does not consider the possible interfacial failure mode although the contribution of all stresses to intralaminar are addressed. Interlaminar delamination and fiber-matrix debonding may take place following transverse cracking or fibre breakage. However, we have not taken the interface effect into consideration in current model and thus we cannot exactly show how it affects the results in this paper. The work of improving the model would be done in the future.

Declaration of Competing Interest

The authors declare that they have no known competing financial interests or personal relationships that could have appeared to influence the work reported in this paper.

Acknowledgment

This work was funded by the National Natural Science Foundation of China (51905264, 11972185), by the China Postdoctoral Science Foundation Funded Project (2019M661818, 2019M650115), by the New Faculty Foundation of NUAA (1001-YAH19069), by the Fundamental Research Funds for the Central Universities (NP2017401), and by the Priority Academic Program Development of Jiangsu Higher Education Institutions.

References

[1] Hashin Zvi. Failure criteria for unidirectional fiber composites. J Appl Mech 1980;47(2):329–34.
[2] Puck A, Schurmann H. Failure analysis of FRP laminates by means of physically based phenomenological models. Compos Sci Technol 1998;58(7):1633–62.
[3] Hinton MJ, Kaddour AS, Soden PD. A comparison of the predictive capabilities of current failure theories for composite laminates, judged against experimental evidence. Compos Sci Technol 2002;62(12–13):1725–97.
[4] Soden PD, Kaddour AS, Hinton MJ. Recommendations for designers and researchers resulting from the world-wide failure exercise. Compos Sci Technol 2004;64(3–4):589–604.
[5] Kaddour AS, Hinton MJ, Smith PA, Shuguang Li. The background to the third world-wide failure exercise. J Compos Mater 2012;46:2283–94.
[6] Pinho ST, Iannucci L, Robinson P. Physically based failure models and criteria for laminated fibre-reinforced composites with emphasis on fibre kinking. Part i. Devel. Compos Part A: Appl Sci Manuf 2006;37(1):63–73.
[7] Davila Carlos G, Camanho Pedro P, Rose Cheryl A. Failure criteria for FRP laminates. J Compos Mater 2005;39(4):323–45.
[8] Schultheisz Carl R, Waas Anthony M. Compressive failure of composites, part i: testing and micromechanical theories. Progress Aerospace Sci 1996;32(1):1–42.
[9] Camanho Pedro P, Dávila Carlos G, Pinho Silvestre T, Iannucci Lorenzo, Robinson Paul. Prediction of in situ strengths and matrix cracking in composites under transverse tension and in-plane shear. Compos Part A: Appl Sci Manuf 2006;37(2):165–76.
[10] Van der Meer FP, Sluys LJ, Hallett SR, Wisnom MR. Computational modeling of complex failure mechanisms in laminates. J Compos Mater 2012;46(5):603–23.
[11] Thai Chien H, Ferreira AJM, Bordas Stéphane Pierre Alain. Timon Rabczuk, and Hung Nguyen-Xuan. Isogeometric analysis of laminated composite and sandwich plates using a new inverse trigonometric shear deformation theory. Eur J Mech-A/Solids 2014;43:89–108.
[12] Catalanotti G, Camanho PP, Marques AT. Three-dimensional failure criteria for fiber-reinforced laminates. Compos Struct 2013;95:63–79.
[13] Abir MR, Tay TE, Ridha M, Lee HP. Modelling damage growth in composites subjected to impact and compression after impact. Compos Struct 2017;168:13–25.
[14] Tsai Stephen W, Wu Edward M. A general theory of strength for anisotropic materials. J Compos Mater 1971;5(1):58–80.
[15] Hashin Zvi. Analysis of composite materials-a survey. J Appl Mech 1983;50(3):481–505.
[16] Soden PD, Hinton MJ, Kaddour AS. Biaxial test results for strength and deformation of a range of e-glass and carbon fibre reinforced composite laminates: failure exercise benchmark data. Compos Sci Technol 2002;62(12–13):1489–514.
[17] Puck A, Kopp J, Knops M. Guidelines for the determination of the parameters in puck's action plane strength criterion. Compos Sci Technol 2002;62(3):371–8.
[18] Matthias Deuschle H, Kröplin Bernd-H. Finite element implementation of puck's failure theory for fibre-reinforced composites under three-dimensional stress. J Compos Mater 2012;46(19–20):2485–513.
[19] Camanho PP, Arteiro A, Melro AR, Catalanotti G, Vogler M. Three-dimensional invariant-based failure criteria for fibre-reinforced composites. Int J Solids Struct 2015;55:92–107.
[20] Reinoso Jose, Catalanotti Giuseppe, Blázquez Antonio, Areias Pedro, Camanho PedroP, París Frederico. A consistent anisotropic damage model for laminated fiber-reinforced composites using the 3d-version of the puck failure criterion. Int J Solids Struct 2017;126:37–53.
[21] Talreja Ramesh. Assessment of the fundamentals of failure theories for composite materials. Compos Sci Technol 2014;105:190–201.
[22] Pascoe John-Alan, Pimenta Soraia, Pinho Silvestre T. Interlocking thin-ply reinforcement concept for improved fracture toughness and damage tolerance. Compos Sci Technol 2019:107681.
[23] Wehrkamp-Richter Tobias, De Carvalho Nelson V, Pinho Silvestre T. Predicting the non-linear mechanical response of triaxial braided composites. Compos Part A: Appl Sci Manuf 2018;114:117–35.
[24] Mesquita Francisco, Swolfs Yentl, Lomov Stepan V, Gorbatikh Larissa. Ply fragmentation in unidirectional hybrid composites linked to stochastic fibre behaviour: A dual-scale model. Compos Sci Technol 2019;181:107702.
[25] Liu Qiang, Gorbatikh Larissa, Lomov Stepan V. A combined use of embedded and cohesive elements to model damage development in fibrous composites. Compos Struct 2019;223:110921.
[26] Rohwer Klaus. Predicting fiber composite damage and failure. J Compos Mater 2015;49(21):2673–83.
[27] Hinton MJ, Sam Kaddour A, Soden Peter D. Failure criteria in fibre reinforced polymer composites: the world-wide failure exercise. Elsevier; 2004.
[28] Knops Martin. Analysis of failure in fiber polymer laminates: the theory of Alfred Puck. Springer Science & Business Media; 2008.
[29] Wiegand J, Petrinic N, Elliott B. An algorithm for determination of the fracture angle for the three-dimensional puck matrix failure criterion for ud composites. Compos Sci Technol 2008;68(12):2511–7.
[30] Jiefei Gu, Chen Puhui. Extension of puck's inter fibre fracture (iff) criteria for ud composites. Compos Sci Technol 2018;162:79–85.
[31] Garrett KW, Bailey JE. Multiple transverse fracture in 90 cross-ply laminates of a glass fibre-reinforced polyester. J Mater Sci 1977;12(1):157–68.
[32] Dvorak George J, Laws Norman. Analysis of progressive matrix cracking in composite laminates ii. first ply failure. J Compos Mater 1987;21(4):309–29.
[33] Chang Fu-Kuo, Lessard Larry B. Damage tolerance of laminated composites containing an open hole and subjected to compressive loadings part i: analysis. J Compos Mater 1991;25(1):2–43.
[34] Wang J, Karihaloo BL. Optimum in situ strength design of composite laminates. part i: in situ strength parameters. J Compos Mater 1996;30(12):1314–37.
[35] Wang J, Karihaloo BL. Optimum in situ strength design of laminates under combined mechanical and thermal loads. Compos Struct 1999;47(1–4):635–41.
[36] Laffan MJ, Pinho ST, Robinson P, Iannucci L. Measurement of the in situ ply fracture toughness associated with mode i fibre tensile failure in frp. part i: data reduction. Compos Sci Technol 2010;70(4):606–13.
[37] Laffan MJ, Pinho ST, Robinson P, Iannucci L. Measurement of the in situ ply fracture toughness associated with mode i fibre tensile failure in frp. part ii: Size and lay-up effects. Compos Sci Technol 2010;70(4):614–21.
[38] Yamada SE, Sun CT. Analysis of laminate strength and its distribution. J Compos Mater 1978;12(3):275–84.
[39] Dong H, Wang J, Karihaloo BL. An improved puck's failure theory for fibre-reinforced composite laminates including the in situ strength effect. Compos Sci Technol 2014;98:86–92.
[40] Catalanotti G. Prediction of in situ strengths in composites: Some considerations. Compos Struct 2019;207:889–93.
[41] Rotem A. Prediction of laminate failure with the rotem failure criterion. Compos Sci Technol 1998;58(7):1083–94.
[42] Sun CT, Tao Jianxin. Prediction of failure envelopes and stress/strain behaviour of composite laminates. Compos Sci Technol 1998;58(7):1125–36.
[43] Schirmaier FJ, Weiland J, Kärger Luise, Henning Frank. A new efficient and reliable algorithm to determine the fracture angle for puck's 3d matrix failure criterion for ud composites. Compos Sci Technol 2014;100:19–25.
[44] Thomson Daniel M, Cui Hao, Erice Borja, Hoffmann Justus, Wiegand Jens, Petrinic Nik. Experimental and numerical study of strain-rate effects on the iff fracture angle using a new efficient implementation of puck's criterion. Compos Struct 2017;181:325–35.
[45] Yerramalli Chandra S, Waas Anthony M. A nondimensional number to classify composite compressive failure. J Appl Mech 2004;71(3):402–8.
[46] Rosen B Walter. Mechanics of composite strengthening. Fiber Composite Materials. American Society for Metals; 1965. p. 37–75.
[47] Argon AS. Fracture of composites. Treatise Mater Sci Technol 1972;1:79–114.
[48] Gutkin Renaud, Costa Sérgio, Olsson Robin. A physically based model for kink-band growth and longitudinal crushing of composites under 3d stress states accounting for friction. Compos Sci Technol 2016;135:39–45.
[49] Swanson SR, Messick MJ, Tian Z. Failure of carbon/epoxy lamina under combined stress. J Compos Mater 1987;21(7):619–30.
[50] Swanson Stephen R, Qian Yibo. Multiaxial characterization of t800/3900-2 carbon/epoxy composites. Compos Sci Technol 1992;43(2):197–203.
[51] Daniel Isaac M, Luo Jyi-Jiin, Schubel Patrick M, Werner Brian T. Interfiber/interlaminar failure of composites under multi-axial states of stress. Compos Sci Technol 2009;69(6):764–71.
[52] Hahn Hong T, Tsai Stephen W. Introduction to composite materials. CRC Press; 1980.